ASTRONOMY & ASTROPHYSICS
SUPPLEMENT SERIES

*Astron. Astrophys. Suppl. Ser.* **92**, 267-289 (1992)



# The Solar Wind Ion Composition Spectrometer

G. Gloeckler[1], J. Geiss[2], H. Balsiger[2], P. Bedini[3], J.C. Cain[3], J. Fischer[2], L.A. Fisk[4], A.B. Galvin[3], F. Gliem[5], D.C. Hamilton[3], J.V. Hollweg[6], F.M. Ipavich[3], R. Joos[2], S. Livi[7], R. Lundgren[3], U. Mall[2], J.F. McKenzie[7], K.W. Ogilvie[8], F. Ottens[8], W. Rieck[5], E.O. Tums[3], R. von Steiger[2], W. Weiss[7] and B. Wilken[7]

[1] Department of Physics and IPST, University of Maryland, College Park, Maryland, USA
[2] Physikalisches Institut, Universität Bern, Bern, Switzerland
[3] Department of Physics, University of Maryland, College Park, Maryland, USA
[4] Office of Space Science and Applications, National Aeronautics and Space Administration, Washington, DC, USA
[5] Institut für Datenverarbeitende Anlagen, Technische Universität Braunschweig, Braunschweig, Germany
[6] Department of Physics, University of New Hampshire, Durham, New Hampshire, USA
[7] Max-Planck-Institut für Aeronomie, Katlenburg-Lindau, Germany
[8] National Aeronautics and Space Administration/Goddard Space Flight Center, Greenbelt, Maryland, USA

*Received April 11; accepted September 16, 1991*

**Abstract.** — The Solar Wind Ion Composition Spectrometer (SWICS) on Ulysses is designed to determine uniquely the elemental and ionic-charge composition, and the temperatures and mean speeds of all major solar-wind ions, from H through Fe, at solar wind speeds ranging from 175 km/s (protons) to 1280 km/s $(Fe^{8+})$. The instrument, which covers an energy per charge range from 0.16 to 59.6 keV/e in ~ 13 min, combines an electrostatic analyzer with post-acceleration, followed by a time-of-flight and energy measurement. The measurements made by SWICS will have an impact on many areas of solar and heliospheric physics, in particular providing essential and unique information on: (i) conditions and processes in the region of the corona where the solar wind is accelerated; (ii) the location of the source regions of the solar wind in the corona; (iii) coronal heating processes; (iv) the extent and causes of variations in the composition of the solar atmosphere; (v) plasma processes in the solar wind; (vi) the acceleration of energetic particles in the solar wind; (vii) the thermalization and acceleration of interstellar ions in the solar wind, and their composition; and (viii) the composition, charge states and behavior of the plasma in various regions of the Jovian magnetosphere.

**Key words:** interplanetary medium — Jupiter — artificial satellites space probes — sun: solar wind.

## 1. Introduction.

Knowledge of the solar wind elemental and ionic-charge compositions, and their variabilities, is essential for our understanding of the physics of the solar wind, the solar atmosphere, and the Sun itself. Measurements of its composition and the mean speeds, kinetic temperatures and charge-state distributions of its major ions under the varying solar-wind conditions and flows will reveal the conditions and processes occurring in the regions where it is accelerated. Such measurements will also provide new information about the elemental composition of the solar atmosphere and processes that lead to variations in this composition, and they will enable us to characterize and study plasma processes occurring in the heliosphere.

*Send offprint requests to*: G. Gloeckler.

The He/H ratio in the solar wind has now been measured for nearly thirty years and found to be quite variable (e.g. Bame *et al.* 1977), ranging from a fraction of a percent to 35%. Electrostatic deflection analyzer plasma detectors can provide composition measurements of major heavy-ion species (O, Si, and Fe), but only under favorable solar-wind conditions (Bame *et al.* 1979). Foil detectors placed on the lunar surface during the Apollo 11, 12, and 14-16 missions provided important measurements of the noble-gas elements in the solar wind and their isotopes (Geiss 1973). Since the late 1970s a magnetic mass spectrometer has been operated on board the ISEE-3/ICE spacecraft, making it possible to study the elemental composition and charge states of major solar-wind ions under less restrictive solar-wind conditions (Coplan *et al.* 1978) (Ogilvie & Vogt 1980).

More recently, a time-of-flight instrument, similar to the one described in this paper, was flown on the AMPTE

spacecraft (Gloeckler *et al.* 1985). During the occasional excursions of this spacecraft into the magnetosheath, the thermalized solar wind gas in that region could be analyzed, providing for the first time unequivocal information on carbon and magnesium in the solar wind (Gloeckler & Geiss 1989).

However, important questions concerning the solar wind composition still remain open, not only at elevated solar latitude, but also in the ecliptic. Elements like carbon or magnesium have not yet been thoroughly studied, the information on charge states is largely confined to oxygen and iron. Systematic measurements of the composition and charge states in high-speed streams are lacking.

The Ulysses mission presents a truly unique opportunity to investigate many of the outstanding and fundamental problems of solar-wind physics using advanced instruments (see Wenzel *et al.* 1991). The spacecraft's out-of-ecliptic trajectory will add a new dimension to these studies, since the three-dimensional properties of the corona and of the solar wind will be observed for the first time (Geiss & Bochsler 1986). The capability of the SWICS to measure the elemental and charge state compositions of ions (Gloeckler *et al.* 1983) will also provide the first detailed charge state and species information for the hot Jovian plasma and its suprathermal component.

A preliminary look at the post-launch data reveals that the Solar Wind Ion Spectrometer experiment on Ulysses will provide comprehensive elemental and ionic-charge composition measurements of solar wind ions from H through Fe, of interstellar ions, and of the Jovian plasma during Ulysses' Jupiter flyby. The instrument's design, fabrication and testing was a collaborative effort by five institutes: the University of Maryland, the University of Bern, the Max-Planck-Institut für Aeronomie, the Technical University at Braunschweig, and the Goddard Space Flight Center. In the following sections we will outline the scientific objectives of our investigation and describe the SWICS instrument and its characteristics and response in some detail.

## 2. Scientific objectives.

Our investigation on Ulysses will address a number of fundamental problems. These will include studies of: (a) solar-wind acceleration and flow, (b) the composition of the solar atmosphere, (c) plasma processes in the solar wind, (d) interstellar ions, and (e) the composition of the Jovian plasma. On a pioneering mission such as Ulysses and with an advanced instrument such as the SWICS, we will undoubtedly also discover solar, heliospheric and Jovian phenomena whose existence cannot be anticipated from our present perspective.

### 2.1. Studies of solar phenomena.

A major scientific objective of the Ulysses mission is to undertake a systematic study of the flow of the solar wind over the poles of the Sun. At such high latitudes, the solar wind is expected to be less complex and therefore easier to understand than other solar-wind flows in the heliosphere. The flow, originating from a semi-steady coronal hole at each pole, is expected to be reasonably constant in speed and unencumbered by the stream-stream interactions that complicate the flow at lower latitudes. By making detailed measurements of the elemental and ionic-charge composition of the solar wind, and of the flow properties of solar-wind ions over the poles as well as at other heliographic latitudes, we will obtain essential information on the conditions characterizing, and the physical processes operating in the region of the corona where most of the solar-wind acceleration occurs. The solar-wind acceleration region lies relatively high in the corona (a few to several solar radii from the Sun's center), where the density is very low (especially in coronal holes). Spectroscopic measurements at these high solar altitudes are very difficult to obtain. In contrast, an abundance of information regarding the acceleration region is available from measurements of solar-wind ions. Indeed, it is quite convenient that the very particles whose acceleration and flow are being studied carry the needed information with them in their composition and behavior.

More specifically, our measurements with the SWICS will contribute to our knowledge of coronal heating and of coronal conditions as well as processes affecting solar-wind acceleration, by providing information on:

(a) Electron temperature and temperature gradient in the region of the corona (including magnetically closed regions in which mass-ejection coronal transients appear to originate) where the observed solar wind is accelerated. This information is obtained by comparison of the measured distribution of ionization states of C, O, Mg, Si, and Fe.

(b) Physical processes in the acceleration region (e.g. ion heating by wave-particle interactions, acceleration by frictional coupling) obtained from measurements of the composition, temperature, and mean speeds of heavy solar wind ions.

(c) Locations of the sources of the solar wind provided by composition and charge-state measurements of solar wind heavy ions at different latitudes.

(d) Compositional variations in the solar atmosphere provided by composition measurements, including for the first time elements like carbon, magnesium and calcium, over a wide range of solar latitudes and for all solar wind flow conditions.

(e) Average solar abundances obtained from comprehensive composition and charge-state measurements of solar wind ions.

### 2.2. Plasma and acceleration processes in the solar wind.

Plasma processes in the solar wind are expected to vary with latitude. At low latitudes, where effects of solar rotation are important, stream-stream interactions and the spiral nature of the heliospheric magnetic field have a controlling influence on the plasma processes. In contrast, at high latitudes stream-stream interactions should be much weaker, and the fields radial. It may also be that the more rapid decrease with distance of the radial magnetic field over the solar poles results in a higher $\beta$ plasma (ratio of thermal to magnetic pressure) than near the ecliptic plane.

Our measurements of the kinetic temperatures of solar-wind ions will provide an important probe of the interplanetary plasma processes that occur as a function of latitude. The response of the kinetic temperatures of solar-wind ions with different charge/mass ratios can be used to study the dominant instabilities which are being excited during stream-stream interactions, or by heat-flux instabilities, or by other processes.

Detailed studies of acceleration processes in the solar wind which lead to the ~MeV/nucleon particles observed in interplanetary space will be possible with the SWICS. Measurements of suprathermal tails of proton, $He^{++}$, $C^{6+}$, $O^{6+}$, and $Fe^{7+}$ to $Fe^{9+}$ energy spectra, and comparison of compositions and charge-state distributions of solar wind and accelerated ions will reveal whether these ions are accelerated directly out of the local solar wind or have a different source of origin, and will indicate how the acceleration and propagation mechanisms depend on particle rigidity. Stream-stream interactions, which are the most likely candidates for the acceleration of these MeV ions, should vary markedly with latitude making these studies especially interesting and unique with Ulysses.

### 2.3. Interstellar ions.

Interstellar neutral gas, which probably consists mainly of H, He, N, O, and Ne, is swept into the heliosphere by the motion of the Sun through the interstellar medium. In the heliosphere these interstellar atoms are singly ionized by photo-ionization from solar UV and by charge exchange with the solar wind, and are then convected outward by the solar wind as they gyrate about the heliospheric magnetic field. The speed of these pick-up ions in the spacecraft frame should range between approximately zero and twice the solar-wind speed.

On Ulysses, interstellar He will be available for study throughout the mission, since neutral interstellar He can penetrate to within ~0.5 AU. Other interstellar neutrals such as O and Ne will partially penetrate to within a few AU of the Sun, and thus should also be seen with the SWICS near 4 to 5 AU.

The initial distribution of the interstellar ions, immediately following their ionization, tends to be quite unstable. How fast and by what mechanism these ions are accommodated into the main solar wind gas remains largely unexplored and will be studied using measurements provided by SWICS which can readily identify these pick-up ions and measure their energy spectra.

### 2.4. Jovian studies.

We expect to obtain important new information concerning the composition of the thermal and suprathermal plasma in the Jovian magnetosphere and to make the first direct ionization state measurements. This information addresses questions of the relative strengths of the various plasma sources, and plasma heating, acceleration, and transport processes within Jupiter's magnetosphere. SWICS may also shed light on the question of the origin (solar wind or Jovian) of suprathermal and energetic ions observed by Voyager 1 and 2 upstream of the Jovian bow-shock. Because of the nature of the encounter trajectory, the SWICS scan will include the corotation direction outbound but not inbound. Therefore, inbound only the hot plasma and suprathermal components ($kT_{hot} \sim 30$ keV from the LECP experiment on Voyager [Krimigis *et al.* 1979]) will be sampled while outbound the cold corotating ions will be observed as well.

The SWICS energy per charge range of 0.16-60 keV/e overlaps that of the Voyager instrumentation and fills the keV/e to 30 keV gap which existed between the Voyager Plasma Science (PLS) and Low Energy Charged Particle (LECP) experiments. It will provide the first and for a long time the only detailed charge state and species information for the hot plasma and suprathermal components.

Among the specific questions which will be addressed by SWICS is the makeup of the ions that originate from Io, one of the strongest Jovian plasma sources identified by the presence of sulfur, oxygen, and sodium ions. By determining mass as well as mass per charge, SWICS can help resolve ambiguities inherent in the Voyager measurements which could not distinguish between e.g. $O^+$, and $S^{++}$, and between $O^+$, and $O^{++}$. Although SWICS is not expected to make high resolution measurements in the inner magnetosphere because of background considerations, its measurements of Iogenic ions in the outer magnetosphere will shed light on relative charge state and chemical abundances. SWICS will also search for molecular ion products arising both from $SO_2$ and $H_2O$. Products of $H_2O$ would be evidence of plasma originating from the icy Jovian satellites. A determination of the abundance of $H_2^+$ and $H_3^+$ is important in evaluating the relative source strength of the ionosphere compared to Io and the solar wind. The discovery of these molecular ions by Voyager at energies above 0.5 MeV/nucleon (Hamilton *et al.*, 1980),

established the Jovian ionosphere as an important plasma source.

Energetic ion increases in the tens of keV range, observed upstream of the bowshock at Earth and by Voyager 1 and 2 at Jupiter (e.g. Ipavich *et al.* 1981, Zwickl *et al.* 1980), (e.g. Lee 1982) are believed to be either solar wind ions accelerated at the bow shock by the first-order Fermi mechanism, or particles leaking from the magnetosphere with little additional acceleration (e.g., Krimigis *et al.* 1985). The resolution of this controversy will come from high resolution composition and charge state measurements made by SWICS. Heavy ions (e.g. O, S, and Fe) will be distinguished from protons, and high-charge state heavy ions from the solar wind can be distinguished from the low charge state heavy ions of magnetospheric origin. Voyager composition measurements started at much too high an energy ($\sim$ 200 keV/nucleon) to make the definitive composition measurements and Galileo measurements will not give charge state information.

## 3. Instrument description.

### 3.1. Principle of operation.

The SWICS sensor is based on the technique of particle identification using a combination of electrostatic deflection, post-acceleration, and a time-of-flight (TOF) and energy measurement (Gloeckler 1977) (Gloeckler & Hsieh 1979). Figure 1 shows schematically the operating principle of the sensor and the functions of the five basic sensor elements employed:

- Ions of kinetic energy $E$, mass $m$ and charge (ionization state) $q$ enter the sensor through a large area, multi-slit *collimator* which selects proper entrance trajectories for the particles.
- The *electrostatic deflection analyzer* serves as an energy-per-charge ($E/q$) filter, allowing only ions within a given energy-per-charge interval (determinded by a stepped deflection voltage) to enter the TOF vs Energy system.
- Ions are *post-accelerated* by a $\sim$ 30 kV potential drop just before entering the TOF vs Energy system. The energy they gain is sufficient to be measured adequately by the solid-state detectors, which typically have a $\sim$ 30 keV energy threshold. An energy measurement is essential for determining the elemental composition of an ion population and ions with energies below $\sim$ 30 keV must be accelerated if their mass is to be identified.
- In the *time-of-flight* system the velocity of each ion is determined by measuring the travel time $\tau$ of the particle between the start and stop detectors separated by a distance of 10 cm.
- The particle identification is completed by measuring the residual *energy* of the ions in a conventional low-noise solid-state detector.

From simultaneous measurements of the time-of-flight $\tau$ and residual energy $E_{\rm meas}$, and a knowledge of the deflection system voltage and hence the $E/q$, and of the post-acceleration voltage $V_{\rm a}$, we can determine the *mass* ($m$), charge *state* ($q$) and incident *energy* ($E$) of each ion as follows:

$$m = 2(\tau/d)^2\,(E_{\rm meas}/\alpha)$$
$$m/q = 2(\tau/d)^2\,(V_{\rm a} + E'/q) \approx 2(\tau/d)^2 V_{\rm a}$$
$$q = (E_{\rm meas}/\alpha)\,/\,(V_{\rm a} + E'/q) \approx (E_{\rm meas}/\alpha)\,/V_{\rm a}$$
$$E = q.(E/q)$$

where $d$ is the flight path. $E'/q$ takes account of the small energy loss of ions in the thin foil of the start-time detector (Ipavich *et al.* 1982) and $\alpha$ ($<1$) is the nuclear defect in solid-state detectors (Ipavich *et al.* 1978). The approximate expressions for $q$ and $m/q$ hold for typical solar wind ions.

### 3.2. The instrumentation.

The SWICS experiment consists of three separately mounted units which are electronically interconnected as shown schematically in Figure 2. The three units are the Sensor, designated GLG-2A, the Post Acceleration Power Supply (PAPS), called GLG-2B, and the Data-Processing Unit (DPU), labelled GLG-1. These units, indicated in Figure 2 by solid boxes, in turn contain various subsystems which will be described more fully below. The subsystems and the institutes responsible for their design, fabrication and testing are also shown in Figure 2.

#### 3.2.1. *Sensor.*

A simplified cross-section of the SWICS sensor GLG-2A, consisting of the deflection analyzer and the high-voltage bubble, is shown in Figure 3. The cylindrical-shaped high-voltage bubble, to which a post-acceleration voltage of up to 30 kV may be applied, contains the TOF telescope and a proton-alpha particle detector, the analog electronics and the sensor power supplies. Each of these subsystems is supported by a G-11 insulator bulkhead and enclosed by a machined-aluminium container with its outer, parylene-coated surface separated from the parylene-coated inner surface of the outer housing by a 6 mm vacuum gap. The ultra-clean TOF compartment is physically isolated from the bubble electronics, with venting provided through the entrance slits and the collimator-deflection system. Digital signals are transferred to the DPU across the 6 mm gap by six opto-couplers. The opto-coupler openings in the housings also serve as venting ports for the sensor electronics and power supplies. Power is supplied to the high-voltage bubble by means of an isolation transformer

through a six-pin, high-voltage feedthrough (not shown) connected to the upper compartment. The photograph of the sensor (Fig. 4) shows the outer configuration of the cylindrical bubble housing, the opto-coupler box, and the deflection system with collimator opening covered by a dust/acoustic protective cover which swings open after launch. The gold-plated, cylindrically-shaped container houses the − 30 kV supply. The sensor is mounted on the earth-oriented side of the spacecraft platform, in the same orientation as shown in the photograph.

*Deflection analyzer.* The three-dimensional configuration of the deflection analyzer may be visualized by revolving the cross-sectional view shown in Figure 3 by 69° about the symmetry axis of the co-axial cylindrical containers. A single conical collimator services the two separate deflection regions of the analyzer. The multi-slit collimator is similar in construction to collimators on our ISEE instruments (Hovestadt *et al.* 1978) and the AMPTE instrument (Gloeckler *et al.* 1985), and allows us to extend the upper energy limit of our analyzer system while maintaining a reasonably large geometrical factor ($\sim 10^{-2}$ cm$^2$). The widths of the individual channels in the collimator are such as to limit dispersions in the analyzer and flight-path differences in the TOF system to <0.5%. The two inner deflection plates are connected to separate outputs of a variable voltage supply housed immediately below the deflection system (Fig. 3) which increments the deflection voltage of both plates simultaneously in logarithmic steps. The maximum voltages on the upper and lower deflection plates are + 1 kV and + 6 kV, respectively. Serration, black-coating and light traps are used to eliminate reflection of visible and UV radiation into the TOF system. Figure 5 shows a top view of the sensor with the electrostatic deflection plates and collimator plates exposed.

The smaller (upper) of the two deflection analyzer regions (proton/helium channel) normally covers an energy range from 0.16 to 14 keV/charge, has a resolution of ~ 4% and will routinely analyze solar-wind protons, He and heavier ions. These ions will be post-accelerated and will be counted by a single rectangular solid-state detector at two threshold levels (20-45 keV, and above 45 keV) corresponding to the energies of post-accelerated solar-wind protons (~ 30 keV) and post accelerated He and heavier ions (≥60 keV). As the voltage is stepped over the full range, this system provides separate $E/q$ spectra for solar-wind protons, and for solar-wind He plus heavier elements, allowing us to determine in a simple manner, *and at all* solar-wind temperatures, the bulk speed, density and temperature of $H^+$ and $He^{++}$ in the solar wind.

The larger (lower) deflection analyzer (main channel) has a ~ 5% energy/charge resolution and is used for the full $m$ vs $m/q$ analysis of solar-wind He and heavier ions and of suprathermal ions, in the range 0.65-60 keV/charge. The TOF vs $E$ system is placed behind the exit slit of the analyzer and inside the high-voltage bubble (Fig. 3). At any given voltage step, the analyzer passes ions that have equal (to within the 5%) energy per charge. These ions are then post-accelerated and their mass, charge state and energy measured by the TOF vs $E$ system as described below.

*Time-of-flight vs energy system.* An important advantage of the TOF technique which *measures* the velocities of ions over a system which *selects* a narrow range of velocities (using, for example, crossed electric and magnetic fields) is that stepping over a velocity range is not required in our instruments. The TOF system accepts a wide range of velocities (or $m/q$ ratios) simultaneously, resulting in factors of 10 to 20 increases in both the time resolution and sensitivity. A second advantage is that coincidence measurements used in TOF systems reduce background levels many orders of magnitude below the typical $10^{-2}$ to 1 count/s background measured in, for example, the singles rates of solid-state detectors on a typical spacecraft.

Figure 6 shows the cross-section of the SWICS TOF vs $E$ assembly consisting of a "start" and "stop" detector 10 cm apart. The start and stop signals are derived from secondary electrons (Gloeckler & Hsieh 1979) that are released with a mean energy of a few eV when an ion enters or leaves a solid surface. The surface material used for the start detector is a thin foil (~ 3 $\mu$g/cm$^2$ carbon foil supported on a 90% transmission nickel grid), and for the stop detector the gold front surface of the Au-Si solid-state detector. The secondary electrons from the start and stop detectors are accelerated to ~ 1 kV and then deflected by a system of acceleration gaps and deflection surfaces as shown in Figure 6 and strike the respective Micro Channel Plate assembly, each of which consists of a rectangular, curved-channel MCP. A common supply (1 kV) is used to both accelerate and deflect the electrons. The output signals from the start and stop MCP assemblies are impedance matched and capacitively coupled across ~ 4 kV in order to keep the foil and solid-state detector at local ground potential. The MCPs are normally biased at ~ 3 kV to operate at a gain of $2 \times 10^6$. This bias voltage (and hence the gain) is adjustable by ground command.

The top view of the TOF vs energy telescope (Fig. 5) shows the positions of the start and stop MCPs, the three solid-state detectors, and the curved carbon foil. The wide field-of-view and the three detectors are necessary to provide look directions towards the Sun over the entire 0° to 60° range of Sun-spacecraft-Earth angles. The slight difference in the flight path of the secondary electrons introduces a timing uncertainty of <0.2 ns FWHM, which is smaller than the <0.5 ns FWHM resolution of the analog electronics. Ions are practically unaffected by the electric fields of the TOF assembly, because of their higher energy. The path length dispersion $\Delta d/d$ for ions is negligible in

the plane of Figure 6 and <0.005 FWHM in the other direction (Fig. 5).

The residual energy is measured by one of the three rectangular solid-state detectors. Table 1 gives additional details for the SWICS TOF vs $E$ assembly. The TOF vs $E$ telescope is shown in Figure 7.

### 3.2.2. *Electronics.*

The SWICS electronics consists of an analog subsystem which is built into the central compartment of the high-voltage bubble (Fig. 3), the DPU and the low-voltage power supply, both housed in the separately mounted GLG-1 box, a variable deflection voltage supply and a detector/MCP bias supply both contained in the sensor (Fig. 3), and the − 30 kV post-acceleration supply in its own cylindrical housing. These subsystems are shown schematically in Figure 2.

*Analog electronics.* A simplified block diagram of the SWICS analog electronics is shown in Figure 8. The main function of these electronics is to measure the time-of-flight $\tau$ and energy $E$ of ions triggering the TOF vs $E$ system. In addition, solar-wind protons and He are quickly identified and counted, and a number of coincidence conditions are established and their occurence counted.

*Time-of-flight measurement.* Each MCP assembly output is capacitively coupled to a fast preamplifier whose function is to accept the 0.9 ns rise-time MCP output signals, shape, amplify, and feed them into a fast timing discriminator using tunnel diodes. The output signals from the start and stop timing discriminator are used as inputs to the Time-to-Amplitude Converter (TAC) which will produce: (a) an output pulse whose amplitude is proportional to the time interval between the trigger of the start and stop discriminators ($T$ signal), and (b) a logic pulse (valid $\tau$) provided the stop signal follows the start signal in <200 ns. The $T$ signal is stretched and pulse-height-analyzed by a 10-bit "Time" Amplitude-to-Digital Converter ($T$-ADC) with a 40 $\mu$s conversion time. The valid $\tau$ logic pulse is used to establish logic conditions and increment counting rates. We have measured the overall timing resolution of the analog electronics to be <0.2 ns when both the start and stop MCP pulses exceed 100 mV.

*Energy measurement.* The output of each of the three solid-state detectors of the TOF telescope is coupled to a low-noise (5 keV FWHM) preamplifier and shaping amplifier (unipolar pulses of 1 $\mu$s duration at 10%). All amplifiers have been hybridized to minimize weight and reduce cross-talk. The output signals of each amplifier chain ($E$-signals) is pulse-height-analyzed by a common 8-bit "Energy" Amplitude-to-Digital Converter ($E$-ADC) and are fed to respective threshold discriminators, whose output is used to identify the triggered detector and to establish logic conditions and increment counting rates.

*Solar-wind proton/helium channel.* The output of the low-noise H/He solid-state detector also goes through a preamplifier/shaping-amplifier chain which then feeds two threshold discriminators (20 keV and 45 keV) whose outputs increment the "proton" and "He" rate and channels, respectively. It is possible to command the instrument into a mode such that the output of the H/He detector is analyzed instead of that of the three main telescope detectors.

*Basic rates, logic conditions, inflight calibrator.* Table 2 lists the data items (rates and pulse-heights) generated by the analog electronics. Pulse-height-analysis of the $T$ signal is normally started by a valid signal whether or not an energy signal is present. Pulse-height-analysis of the $E$ signal normally requires a triple coincidence condition (start-stop and energy). It is possible, however, to change the $T$-ADC analysis logic by ground command to require also a triple coincidence for its analysis. An inflight calibration provides either on command, or at pre-programmed time intervals, a sequence of timing and amplitude pulses which are fed, respectively, to the fast amplifiers or preamplifiers of each MCP or solid-state detector. When the instrument is being calibrated, the trigger logic prevents all except the calibrate pulses from being analyzed.

*Data-processing unit.* The basic data (Time and Energy pulse heights) provided by the SWICS sensor lend themselves to straightforward on-board processing which simplifies ground-based data reduction. The DPU performs this function and provides the interfaces to the SWICS sensor and analog electronics and to the spacecraft (Fig. 2). The other principal functions of the DPU are to: (a) execute fast classification of ions according to the ion mass ($m$) and mass per charge ($m/q$); (b) collect and store count-rate and pulse-height data, determine event priority, and execute appropriate event sequencing, compress the contents of each counting-rate register into an 8-bit floating-point representation, format all data into 8-bit words, and transfer this information to the spacecraft; and (c) perform all necessary control functions for the experiment, accept and execute ground commands, monitor the experiment status, and execute an on-board calibration sequence.

*Fast on-board data processing ($m$ vs $m/q$ classification).* For every ion for which $E$ and $T$ pulse heights are available, the $m$ and $m/q$ are calculated using fast ($\sim$ 50 $\mu$s) look-up-table techniques which establish a correspondence between the measured $T$ and $E$ pulse heights and the stored positions of the $m$ and $m/q$ surfaces in the $T$ vs $E$ parameter space. In order to reduce drastically (by a factor of $\sim$ 100) the excessive storage capacity requirements inherent in a "brute-force" look-up technique (required ROM capacity of $\sim$ 22 Mbits), we use a first-order Taylor expansion for each coarse grid of the $T$ vs $E$ plane, as illustrated in Figure 9 for the mass classification.

The mass $m(T, E)$ of an ion is computed from the $T$ and $E$ pulse heights produced by this ion using

$$m(E,T) = m_0(E_0, T_0) + \partial m/\partial E(E_0, T_0)\,\Delta E + \\ + \partial m/\partial E(E_0, T_0)\,\Delta T$$

where $E_0, T_0$ are the most significant bits of the $E$ and $T$ pulse heights, $\Delta T$ and $\Delta E$ are least significant bits, and $m_0(E_0, T_0)$, $\partial m/\partial E(E_0, T_0)$ and $\partial m/\partial T(E_0, T_0)$ are appropriate elements stored in a ROM look-up table.

*Matrix rates and matrix elements.* The $m$ and $m/q$ values returned by the fast classifier are used to increment appropriate storage elements (MR registers) corresponding to counting rates of selected ion species (Tab. 2), and of the 512 matrix elements contained within the boxed regions of the mass vs mass/charge plane shown in Figure 10.

*Direct Pulse-Height Analysis data and priority selection.* The most detailed information about the composition, arrival directions and energy of ions is contained in the 24-bit PHA words (eight bits for energy, ten bits for TOF, three bits for one of eight sectors, two bits for one of three detectors, and one bit for priority).

The DPU collects and formats the required information for each PHA word, establishes priority categories, and compiles a string of PHA words arranged sequentially such that a balanced ratio of high and low priority events is always telemetered. Three priority categories are defined as shown in Figure 10. Category-I (Range-0) are elements classified to have a mass less than 8.7, category-II (Range-1) are those with mass greater than 8.7, and category-III (Range-2) are low-charge-state heavy elements ($m/q > 3.3$), likely to be interstellar $O^+$, $Ne^+$, etc, which do not trigger the solid-state detectors and hence produce only a TOF pulse height. Such events are labelled "mass-zero" events because only their mass/charge can be measured. Normally, category-I events are assigned lowest priority and category-III events highest priority. Other priority schemes, including a rotating priority, can be implemented by ground command.

Housekeeping data, analog performance parameters, rate data (Tab. 2), eight of the 512 matrix elements and a maximum of 30 (eight at reduced bit rate) PHA events are telemetered once every 12 s (one spin period). Priority selection of the 30 (or 8) telemetered PHA events is accomplished in three steps: (a) the first 30 (or 8) events are accumulated regardless of priority, (b) the next 30 (or 8) events are restricted to middle- and high-priority events and replace the first group of 30 on a one-to-one basis, and (c) the final 30 (or 8) events are restricted to the highest priority, and again replace the second group of 30 on a one-to-one basis. Depending on the event rate, this process may be terminated at any, and within any, of the three steps at the end of the 12 s period between readouts. It should be noted that priority selection affects only the direct pulse-height data.

3.2.3. *Instrument requirements.*

*Mass and power.* The mass of the complete SWICS instrument, including interconnected harness and thermal blankets for GLG-2A and B (sensor and high-voltage supply) is 5584 g, and the total raw power requirement (except for heater power) is 3950 mW (Table 3).

*Telemetry and command.* On-board processing reduces considerably the telemetry that would otherwise be required to send back the information acquired by the SWICS sensor. The telemetry required to transmit the basic rates, matrix rates, $m$ vs $m/q$ elements and direct pulse heights is given in Table 2. The total bit rate is 88 bit/s in the "tracking" mode and 44 bit/s in the storage mode. In addition, five analog performance parameters are read out. The instrument requires three on-off commands (instrument power, post-acceleration supply power, and heater power), three 16-bit command words, and a redundant pair of commands to initiate opening of the acoustic cover.

*Cleanliness and thermal.* Because of the susceptibility of the MCPs and solid-state detectors to contaminants and because of use of thin foils in this experiment a dust/acoustic cover is provided for the sensor. This cover sealed the collimator opening and was commanded to swing open after the spacecraft was injected into its orbit. To avoid damage to the MCPs prior to launch, the instrument was purged continuously with dry nitrogen through ports provided in the sensor.

Thermal-design requirements for the GLG-2A sensor are an orbital temperature of 0°C to −25°C, preferably −10°C to −20°C. The thermal requirements are driven by solid-state-detector operating and survival temperature limits, and are achieved through use of thermal reflecting coatings, blankets and radiators, and two heaters.

3.2.4. *Instrument capabilities and characteristics.*

The SWICS instrument is capable of measuring the solar-wind elemental and charge-state composition under all conceivable solar-wind conditions. The sensitivity and dynamic range of the instrument are such that the mean speeds, temperatures and densitites of all major elements in the solar wind may be determined with a time resolution of 13 min to a few hours.

*Energy range.* The combined energy range of the main channel and the H/He channel extends from 100 eV/e (140 km/s protons) to 60 keV/e (3400 km/s protons; 1285 km/s $Fe^{+8}$). This large dynamic range of 600 in energy per charge will allow us to carry out solar-wind

composition measurements under all possible flow conditions, as well as to study the suprathermal tails of the distribution functions of for example H, He and O. Table 4 lists the energy ranges and resolution (3.65 or 7.44% selectable by command) for the four modes of operation of the SWICS instrument.

*Sensitivity.* The multi-slit collimator used in the SWICS makes it possible to obtain a relatively large geometrical factor ($\sim 10^{-2}$ cm$^2$) and a wide field-of-view without sacrificing the energy resolution of the deflection analyzer. The counting efficiency in the TOF system depends on the degree of scattering of ions in the front foil (most pronounced for low-energy heavy ions) and number of secondary electrons produced by ions at the surface of the foil and solid-state detector (lowest number for higher energy protons). Pre-flight calibrations indicate that the counting efficiency for triple-coincidence analysis is typically in the range 30 to 80% for ions heavier than He in the energy range of the SWICS (depending on the MCP bias level). The efficiencies for counting protons and He are lower; however, the solid state detector in the H/He channel will identify and count H, He and heavier ions with nearly 100% efficiency (at 30 kV post-acceleration).

*Intensity dynamic range.* With the SWICS instrument we are able to achieve an intensity dynamic range of $\sim 10^9$ because: (a) the most intense solar-wind fluxes (protons) are generally measured only in the H/He channel; (b) the rare elements are analyzed in the TOF vs $E$ system with high priority; and (c) the high immunity of background makes it possible to detect and identify rare elements and ions. The largest contributors to background are RTG $\gamma$'s and neutrons, and penetrating ($\geq$10 MeV) solar-flare protons. For example, in a typical solar-flare particle event the flux of >10 MeV protons is $\sim 20$ cm$^{-2}$s$^{-1}$ sr$^{-1}$, which will result in a background counting rate in a *single* detector in excess of 100 count/s. The triple coincidence technique and multi-parameter analysis used in the SWICS reduces the instrumental background due to this source to $\sim 10^{-4}$ count/s in each of the time vs energy matrix elements. In testing a prototype TOF telescope exposed to $\gamma$-ray fluxes of an RTG simulator we found triple-coincidence rates of $\sim 10^{-4}$ count/s. Using integration times of several hours and being able to further correct the detailed PHA data for any residual background, we should be able to measure minimum solar-wind fluxes of between $\sim$1 and 20 cm$^{-2}$ s$^{-1}$ depending on spacecraft orientation. The maximum proton flux of $\sim 10^9$ cm$^{-2}$ s$^{-1}$ we can measure is determined by the peak counting rate of our H/He detector ($5 \times 10^5$ count/s, the proton temperature, and the energy bandwidth and geometrical factor of the deflection analyzer.

*Mass and mass per charge resolution.* We have determined the mass and mass/charge resolution of the SWICS for every major ion species using all known aspects of the instrument. These include effects due to: (a) deflection analyzer system resolution and dispersion; (b) electronic noise in the TOF measurement and path-length dispersion of secondary electrons; (c) path-length differences of ions in the TOF system; (d) energy dispersion associated with nuclear defects in solid-state detectors and electronic noise in the energy measurement; and (e) timing dispersions caused by energy straggling of ions in the carbon foil. These effects which have been measured or are determined by the geometry of the system are combined in quadrature to give the FWHM resolutions in mass, $\Delta(m)$, and mass/charge, $\Delta(m/q)$. Table 5 summarizes the mass and mass/charge resolution in the SWICS for common solar-wind ions (at 30 kV post-acceleration).

*Modes of operation. Voltage cycle mode.* The energy-per-charge dynamic range and step resolution of the instrument are commandable by six predefined voltage cycle modes that are available for the electrostatic deflection analyzer system. A deflection voltage cycle consists of 64 voltage steps, resulting in an instrument duty cycle of approximately 12.8 minutes at spacecraft bit rates of 1024 and 512 bps, and at the nominal spin rate of 12 seconds. (The deflection analyzer voltage steps once per spacecraft spin at these telemetry bit rates). The deflection voltage plates of the Main and H/He channels step in concert, with the H/He channel offset by a factor of four lower in energy per charge from the Main channel. The deflection voltage is automatically stepped down (or up, after step reversal) according to the mode selected by command. Two of the commandable voltage modes cover primarily the suprathermal energy regime (with Main channel energy-per-charge ranges of 59.6-6.3 keV/e and 40.4-4.3 keV/e, respectively). The four operational modes most likely to be used in flight, covering the solar wind energy-per-charge regime, are given in Table 4. For each mode, the corresponding energy-per-charge and velocity ranges for different ion species are given for the Main and H/He channels. Depending upon the mode, the voltage step spacing is either 7.44% or 3.65%, thus providing a choice between finer resolution in the energy-per-charge steps or a larger dynamic range.

*Automatic step reversal mode.* In order to extend the life of the microchannel plates used in the Main channel, the total fluence on the plates is restricted through the use of a commandable "automatic step reversal" in the deflection voltage cycle. This features takes advantage of the fact that the solar wind velocity is roughly the same for all ion species, hence the energy-per-charge spectrum is well-ordered in mass per charge. The SWICS starts a voltage cycle at the highest voltage step (and hence

highest energy per charge) of a given voltage cycle mode. As the deflection system steps down in energy per charge, the minor ions and helium ions are observed before the system steps into the energy-per-charge domain of the high fluence solar wind protons. A maximum allowable counting rate for the start signal microchannel plate is set by ground command, at any one of eight selectable rate-limit values (ranging from 256 to 524, 288 counts per spin). If during one spin the start signal rate (the FSR) exceeds the selected value, the step direction of the deflection voltage cycle is reversed. The deflection voltage is then stepped up until a full cycle of 64 steps is completed (if the highest voltage step is reached before the end of the cycle, the deflection voltage remains in that step until the cycle is completed). An example of the instrument undergoing step reversal under flight conditions is given in Figure 12 (see Sect. 5).

The automatic step reversal assures a conservative level for the total fluence on the microchannel plates. Except under unusual conditions (solar-wind densities in excess of 25 $cm^{-3}$) the typically selected rate limit will not be exceeded until the TOF vs $E$ system completely analyzes He and begins measuring into the proton peak. Because the H/He channel is offset in energy-per-charge from the Main channel by a factor of four, the H/He channel normally steps through the protons as well as helium and the heavier ions before step reversal is initiated by the fluence level measured in the Main channel. The rate-limit condition is overridden automatically once every 64 voltage cycles (about every 14 hours for nominal spin periods and telemetry bit rates of 1024 or 512 bps) to allow a complete spectrum. The Automatic Step Reversal mode can be disabled by ground command.

*Post acceleration power supply mode.* Ions with the correct energy per charge to get through the deflection analyzer system then pass through a commandable potential drop before entering the TOF vs. E system of the instrument. This post acceleration after electrostatic analysis raises the energy of the ion by an amount $V_a q$, which is typically sufficient to trigger the solid state detector and allow energy measurements. There are sixteen commandable post acceleration voltage levels, ranging from 8 kV to 30 kV. The Data Processing Unit can correctly classify ions with post acceleration voltages that are $\geq$15 kV. It can also classify events for $V_a = 0$ (i.e., post-acceleration off) for deflection voltage steps $\geq$ 100 ($E/q \geq$ 15.5 keV/e in the Main channel). This last feature allows a partial recovery of the science data in the event of a failure of the post acceleration power supply. During the early part of the mission (November to December, 1990), the post acceleration level was gradually stepped up to its current level of 22.9 kV. Although this voltage level is insufficient to obtain triple coincidence events on solar wind protons and some fraction of solar wind alphas, it does permit triple coincident information on most minor ions.

*H/He channel pulse height mode.* In the event of a failure of the Main channel's TOF system, there is a partial recovery mode in the experiment that replaces in the telemetry stream the direct pulse height data from the Main channel with direct pulse height data taken from the H/He channel. (Normally, the H/He pulse height data are not transmitted in the telemetry). In this operational mode, one has the standard electrostatic deflection ($E/q$) and total energy ($E$) instrument, combined with post acceleration.

## 4. Instrument calibration.

Thorough calibration of the instrument was critical because the SWICS is a complex detector system which combines three distinct subsystems: (a) the collimator/deflection system (providing $E/q$); (b) the time-of-flight sensor (providing particle velocity); and (c) solid-state detectors (providing total energy). Data from these subsystems must be reliably combined (both by the on board DPU and on the ground) to infer the incident energy, mass, and mass per charge of incoming ions. Calibrations of the SWICS engineering-model (EM), flight spare (FS), flight unit (FU), and refurbished flight unit sensors were performed before flight.

At the time SWICS was being tested no single calibration facility was capable of simulating the solar-wind ions that the sensor is now detecting in space. This would have simultaneously required: low incident $E/q$ (0.1-60 keV/e); high charge states ($q \sim$ 1 to 20); and elements from H through Fe. It was therefore necessary to use several complementary facilities to provide our overall instrument calibration. Particle beam calibrations of the instrument and subsystems were performed using the DC accelerator/mass spectrometer at the University of Bern, the DC accelerator at the MPAe/Lindau, and the Van de Graaff accelerator at Goddard Space Flight Center.

The accelerator at Bern was the only facility at which we calibrated the fully assembled SWICS. Here we measured the efficiencies, geometry factors, energy and angular response of the collimator/deflection system over the full energy per charge range of the sensor. The accelerator facility was ideally suited for SWICS in that it covered an energy range of a few eV to 60 keV/e and provided a large-area, highly parallel beam of ions (Ghielmetti *et al.* 1983). Efficiencies were determined for the microchannel plates for a variety of ion species and for different bias levels of the MCPs. The ion species tested included $H^+$, $H_2^+$, $He^+$, $He^{+2}$, $O^+$, $C^+$, $N^+$, $Ne^{+3}$, $Ar^{+4}$, $Kr^{+4}$. Relative efficiency data for the flight configuration microchannel plates are shown in Figure 11 for Neon.

## 5. Post-launch performance.

The SWICS instrument reached its normal mode of operation in December 9, 1990 following a turn-on sequence that included a gradual increase in the post-acceleration voltage to the present value of 22.9 kV. The experiment is operating in space as designed and is returning data of excellent quality unavailable in previous explorations of the solar wind. In particular, background suppression techniques used to minimize drastically if not eliminate contributions from UV, RTG, etc. have proven to be extremely effective, and the SWICS's capability to resolve all major heavy elements in the solar wind and measure their charge states has now been demonstrated. Below we will provide just a few examples of essentially flight raw data processed on-board by the DPU.

The four panels of Figure 12 show the energy per charge vs time color spectrograms for the H/He channel (top), $He^{++}$, $O^{6+}$, and Si (bottom) respectively. Vertical white bars indicate data gaps, blank areas represent zero counts and the color bar on the right codes the logarithm of counts in a given energy per charge bin. Displays of this type will be produced routinely and are useful for an overview of solar wind flow conditions throughout the mission. In the top panel each $\sim$ 13 minute, 64-step scan from high to low energy per charge shows resolved peaks due to solar wind $H^+$ and $He^{++}$ measured with the solid state detector of the H/He channel. Variations in the bulk speed, density, and kinetic temperature are easily discerned in the data shown in all four panels. Effects due to step reversal are seen in all but especially the three bottom panels. Step reversal occurs when the count rate in the start detector of the time-of-flight system exceeds a value selectable by command (see Sect. 3.2.4). At that time the stepping sequence is reversed; that is, the deflection voltage is sequentially increased until the 64-step cycle is completed. Since step reversal most often occurs before the peak of the proton intensity is reached, some of the low-energy portion of the energy per charge spectrum is retraced for alpha particles and heavier ions in the main (time-of-flight) system. The fraction of the spectrum retraced depends on the mass/charge of the ion and the bulk speed, density and kinetic temperature of protons (see Fig. 12, three bottom panels). Because the proton-alpha channel covers an energy/charge range four times lower than the main channel, protons are measured by that system before (and sometimes after) step reversal, as can be seen in the top panel of Figure 12. The step reversal mode is implemented in order to limit the total counts accumulated in the star microchannel plate durign the five year period of the Ulysses mission.

In Figure 13 we display the differential intensity spectra of $H^+$ and $He^{++}$ respectively, time-averaged over a two day period. The differential fluxes for each ion species are derived from the corresponding matrix rates generated from the data classified by the DPU. The smooth curves represent convected maxwellian distributions each having the same bulk speed of 410 km/s and a temperature/mass, $T/m$, of $13.5\times10^4$K. This single maxwellian is a good fit to the main portion of the measured spectra for each species indicating that these ions have a common bulk speed and kinetic temperature per mass. Notice, however, that the differential spectra of protons and alpha particles have pronounced, non-maxwellian, high-energy tails.

The highest-resolution mass and mass/charge information is derived from the direct pulse-height data. These data are used by the DPU for on-board mass classification and the generation of matrix rates and matrix elements, and a sample of a most 30 direct pulse-height events is transmitted every spin. Thus, fairly long-term averages are required to accumulate enough statistics to reveal the presence of the less abundant heavy ion species. An example of a mass vs mass per charge matrix accumulated over a nine day time period and summed over all voltage steps is shown in Figure 14. Mass and mass/charge values were computed from each pair of energy and time-of-flight pulse-heights using algorithms identical to those employed in the DPU. The color scale was adjusted to reveal the presence of rarer ions. In addition to the more abundant ions $C^{6+}$, $C^{5+}$, $O^{7+}$ and $O^{6+}$, the presence $Ne^{8+}$, $Mg^{10+}$, $C^{4+}$, charge states 7, 8 and 9 of Si, and charge states 7, 8, 9, 10 and 11 of Fe are also visible.

The mass and mass/charge resolution capability of SWICS is illustrated in Figure 15 using matrix element [Fig. 15(a)] and direct pulse-height data [Fig. 15(b), (c), and (d)] summed over all voltage steps during a two day period. In Figure 15(a) the mass distribution for ions with mass/charge values between 1.76 and 2.11 amu/e demonstrates that $C^{6+}$ is clearly resolved from $He^{++}$. Figure 15(b) shows the mass distribution in the mass/charge range of 2.45 to 2.55 amu/e, indicating that $C^{5+}$ ($m/q = 2.4$) and $Ne^{8+}$ ($m/q = 2.5$) are resolved. In Figure 15(c) we show the mass per charge distribution in the mass 8 to 10 amu range. In addition to the three charge states of carbon that are well resolved, some fraction of $O^{6+}$ spills over into the 8 to 10 mass range (see also Fig. 14). Despite this spillover, the excellent mass/charge resolution allows us to easily separate oxygen from carbon. Finally, we show the mass/charge distribution in the 40 to 100 amu mass range in Figure 15(d). It is evident that all charge states of iron are well resolved.

The mass and mass/charge resolution capabilities of SWICS illustrated above make it possible to identify $He^+$ and obtain the energy spectra of these ions. In Figure 16 we show the differential energy spectrum of $He^+$, summed over a seven day period. The sharp cut-off at energy/charge corresponding to twice the solar wind speed measured during this same period gives strong evidence that these are interstellar pick-up ions such as first observed by Möbius *et al.* (1985).

**Acknowledgements.**

The design, development, fabrication, testing and calibration of SWICS would have been impossible without the ingenuity and dedicated efforts of many individuals in the five cooperating institutions. We owe our special thanks to Robert Cates (UMD), who designed portions of and assembled the SWICS sensor, Karl Otto (MPAe), who debugged and tested the compact analog electronics, H. Dinse (TUB), who programmed the DPU and implemented the mass, mass/charge classification scheme, and Charles Moyer (GSFC), who designed and built the BCE hardware. Dornier System fabricated the flight and spare units of the analog electronics and the DPU. For the calibration of the instrument, we are especially grateful to Scott Lasley (UMD), Urs Schwab and Uli Rettenmund (Univ. Bern), and Hartmut Sommer (MPAe). For assisting with the integration of the engineering-model unit in the spacecraft and supporting spacecraft test activities, we thank Uli Rettenmund (Univ. Bern). We gratefully acknowledge the technical assistance and advice provided by W. Frank, P. Caseley, H. Schaap, J.P. Bouchez and G. Tomaschek of ESA/ESTEC. and by M. Agabra and J. Haas at JPL. Our special thanks go to Tom Tomey, George Nickols, and Willis Meeks for their help and encouragement during the time before launch when anomalies found in both instruments had to be fixed.

## References

Bame S.J., Asbridge J.R., Feldman W.C. and Gosling J.T. 1977, J. Geophys. Res. 82, 1487

Bame S.J., Asbridge J.R., Feldman W.C., Fenimore E.E. and Gosling J.T. 1979, Solar Physics 62, 179

Coplan M.A., Ogilvie K.W., Bochsler P.A. and Geiss J. 1978, IEEE Trans. Geosci. Electron. GE16, 185

Geiss J. 1973, Proc 13th Int. Cosmic Ray Conf. 5, 3375

Geiss J. and Bochsler P. 1986, "The Sun and the Heliosphere in Three Dimensions", R.G. Marsden Ed. (D. Reidel Publ. Co.) 173

Ghielmetti A.G., Balsiger H., Baenninger R., Eberhardt P., Geiss J. and Young D.T. 1983, Rev. Sci. Inst. 425

Gloeckler G. 1977, Univ. Maryland Tech. Report, TR-77-043

Gloeckler G. and Hsieh K.C. 1979, Nucl. Instrum. Methods 165, 537

Gloeckler G., Geiss J., Balsiger H., Fisk L.A., Gliem F., Ipavich F.M., Ogilvie K.W., Stüdemann W. and Wilken B. 1983 (ESA Spec. Publ. SP-1050) 77

Gloeckler G., Wilken B., Stüdemann W., Ipavich F.M., Hovestadt D., Hamilton D.C. and Kremser G. 1985, Geophys. Res. Lett. 12, 325

Gloeckler G. and Geiss J. 1989, Proc. Cosmic Abundances of Matter Symposium, AIP Conf. Proc. 183, 71

Hamilton D.C., Gloeckler G., Krimigis S.M., Bostrom C.O., Armstrong T.P., Axford W.I., Fan C.Y., Lanzerotti L.J. and Hunten D.M. 1980, Geophys. Res. Letters 7, 813

Hovestadt D., Gloeckler G., Fan C.Y., Fisk L.A., Ipavich F.M., Klecker B., O'Gallagher J.J., Scholer M., Arbinger H., Cain J.C., Hoefner H., Kuenneth E., Laeverenz P. and Tums T.O. 1978, IEEE Trans. Geosci. Electron. GE-16, 166

Ipavich F.M., Lundgren R.A., Lambird B.A., Gloeckler G. 1978, Nucl. Instrum. Methods 154, 291

Ipavich F.M., Galvin A.B., Gloeckler G., Scholer M. and Hovestadt D. 1981, J. Geophys. Res. 86, 4337

Ipavich F.M., Ma Sung L.S. and Gloeckler G. 1982, Univ. Maryland Tech. Report TR-82-172

Krimigis S.M., Armstrong T.P., Axford W.I., Bostrom C.O., Fan C.Y., Gloeckler G., Lanzerotti L.J., Keath E.P., Zwickl R.D., Carbary J.F., Hamilton D.C. 1979, Science 206, 977

Krimigis S.M., Zwickl R.D. and Baker D.N. 1985, J. Geophys. Res. 90, 3947

Lee M.A., 1982, J. Geophys. Res., 87, 5063

Möbius E., Hoverstadt D., Klecker B., Scholer M., Gloeckler G. and Ipavich F.M., 1985, Nature 318, 426

Ogilvie K.W., Vogt C., 1980, Geophys. Res. Letter, 8, S77

Wenzel et al. 1991, this issue

Zwickl, R.D., Krimigis, S.M., Armstrong T.P. and Lanzerotti L.J., 1980, Geophys. Res. Letters, 7, 453

TABLE 1. *Time-of-flight and energy-system characteristics for the SWICS instrument.*

| Subassembly | Characteristics |
|---|---|
| Time-of-flight assembly (TOF) | |
| Flight path | 10 cm |
| Start element | carbon foil ($3\mu/cm^2$, grid-supported) ($0.4x8\ cm^2$) |
| Stop element | three rectangular solid-state detectors ($1.1 \times 1.3\ cm^2$ active each) |
| Microchannel plates (MCP) | |
| Type | curved channel |
| Size (active) | two rectangular ($1.5 \times 3.7\ cm^2$ each) |
| TOF telescope dispersion | |
| Path length, $\Delta d/d$ | $\leq 0.005$ |
| Secondary electrons | 0.3 ns |
| Energy measurement circuitry | |
| Range | 40-600 keV |
| Electronic noise (FWHM) | 12 keV |
| E-ADC range | 256 channels |
| E-ADC resolution | 2.34 keV/channel |
| Time-of-flight measurement circuitry | |
| Range | 10-200 ns |
| Electronic noise(FWHM) | 0.2 ns |
| T-ADC range | 1024 channels |
| T-ADC resolution | 0.195 ns/channel |

TABLE 2. *SWICS telemetry allocation for data items generated in the analog electronics and DPU.*

| Data item Name | No. of spin | Origin | Corresponding physical parameter | No. of bits per item Per spin* | Per second |
|---|---|---|---|---|---|
| FSR | 1 | AE** | start detector rate | 8 | 0.67 |
| DCR | 1 | AE | start-stop coincidence rate (valid t rate) | 8 | 0.67 |
| TCR | 1 | AE | valid t -solid-state detector (SSD) coincidence rate | 8 | 0.67 |
| MSS | 1 | AE | combined count rate of three main channel SSDs | 8 | 0.67 |
| ACP | 2 | AE | solar-wind proton rate*** | 2 x 8 | 1.34 |
| ACA | 2 | AE | solar-wind helium and heavy-ion rate | 2 x 8 | 1.34 |
| MEX | 8 | DPU | 8 of 512 m vs m/q matrix elements (see Fig. 10)**** | 8 x 8 | 5.36 |
| MRX | 18 | DPU | Counting rate of 18 selected ion species (see Fig. 10)***** | 18 x 8 | 12.06 |
| BRX | 3 | DPU | 3 basic rates for each of 3 priority groups (see Fig. 10) | 3 x 8 | 2.01 |
| PHA****** | 30 | AE | 30 24-bit E and T pulse-height events | 30 x 24 | 60.3 |
| ID | 2 | DPU | ID synch word | 2 x 8 | 1.34 |
| HK | 3 | DPU | Housekeeping data | 3 x 8 | 2.01 |
| | | | | 1056 bit/format | 88 bit/s |

* Voltage is stepped each spin = 12s. At spacecraft data rates lower than 512 bit/s voltage is stepped at a slower rate.

** AE = analog electronics.

*** This rate is sectored into (1) a narrow (typically 45° but adjustable by command) sun-centered sector, and (2) a broad (typically 315°) anti-solar sector.

**** Each of 512 matrix elements is accumulated in one complete voltage cycle = 64 spins or 12.8 min. From these 512 matrix elements an energy-averaged mass-mass/charge composition may be determined.

***** The 18 matrix rates correspond respectively to the following 18 ion species: $H^+$ (E and T), $^4He^{+2}$, $H^+$ (T, no E), $^4He^+$ (T, no E), singly ionised heavy ions ($N^+$, $O^+$, $Ne^+$ ...), $C^{+4.5}$, $C^{+6}$, $N^{+4\ to\ 7}$, $O^{+4\ to\ 6}$, $O^{+7}$, $O^{+7}$, $Ne^{+3\ to\ 10}$, $Mg^{+8\ to\ 12}$, $Si^{+9\ to\ 14}$, $S^{+5\ to\ 16}$, $Fe^{+6\ to\ 8}$ and $Fe^{+9\ to\ 22}$.

****** 30 PHA events are telemetered in −12s in the spacecraft tracking-mode transmission. 8 PHA events are telemetered in −12s in the spacecraft storage mode transmission (512 bit/s).

TABLE 3. *Mass and power for SWICS subsystems.*

| Substystem | Mass(g) | | Power*(mW) | |
|---|---|---|---|---|
| -30kV supply (GLG-2B) | 566 | | 550 | |
| Sensor (GLG-2A) | 3426 | | 1900 | |
| Deflection system and deflection supply | | 1483 | | 400 |
| Analog electronics and bias supply | | 903 | | 1200 |
| Sensor elements and structure | | 1035 | | 300 |
| DPU (GLG-1) | 1233 | | 1500 | |
| DPU | | 1135 | | 900 |
| Low-voltage supply | 120 | | | 600 |
| Thermal blankets | 303 | | | |
| Interconnect cable | 56 | | | |
| TOTAL | 5584 g | | 3950 mW | |

*Average power; peak power 4.8 W.

TABLE 4. *E/Q, solar wind velocity ranges, and resolutions in the four SWICS operating modes.*

| | Mode-0 | Mode-1* | Mode-2 | Mode-3 |
|---|---|---|---|---|
| Energy charge range (keV/e) | | | | |
| Main channel | 0.45-40 | 0.65-60 | 0.45-4.3 | 0.65-6.3 |
| H/He channel | 0.11-10 | 0.16-14 | 0.11-1.0 | 0.16-1.5 |
| Velocity range (km/s) | | | | |
| Main channel | | | | |
| H | 290-2800 | 350-3400 | 290-910 | 350-1100 |
| $He^{++}$ | 210-2000 | 250-2400 | 210-640 | 250-780 |
| $Fe^{+8}$ | 110-1050 | 130-1280 | 110-340 | 130-420 |
| H/He channel | | | | |
| H | 150-1380 | 180-1640 | 150-440 | 180-540 |
| $He^{++}$ | 100-980 | 120-1160 | 100-310 | 120-380 |
| Voltage range (V) | | | | |
| Main channel | 47-4200 | 68-6300 | 47-450 | 68-660 |
| H/He channel | 7-670 | 11-945 | 7-67 | 11-100 |
| Number of voltage steps/cycle** | 64 | 64 | 64 | 64 |
| Voltage step range** | 1-127 (by 2's) | 12-138 (by 2's) | 1-64 | 12-75 |
| Step size (%) | 7.44 | 7.44 | 3.65 | 3.65 |

* Normal mode of operation.
** Voltage is stepped each spin (12s). A voltage cycle consists of 64 steps and is started at the highest voltage step, and then stepped down until the counting rate in the start MCP exceeds a value selectable by command (typically $5 \times 10^4$ count/s). The voltage is then stepped up until the 64 steps are completed.

TABLE 5. *SWICS resolution characteristics for typical solar-wind ions**.

| Element | Mass | Charge | Energy** (keV) | Time-of-flight (ns) | Δ(m/q)/(m/q) (FWHM) | Δm/m (FWHM) |
|---|---|---|---|---|---|---|
| H | 1 | 1 | 19 | 48.7 | 0.054 | 0.742 |
| He | 4 | 2 | 38 | 66.7 | 0.042 | 0.397 |
| C | 12 | 6 | 103 | 66.3 | 0.039 | 0.223 |
| N | 14 | 7 | 117 | 66.3 | 0.039 | 0.224 |
| O | 16 | 6 | 91 | 75.7 | 0.038 | 0.265 |
| Ne | 20 | 8 | 116 | 73.2 | 0.034 | 0.305 |
| Si | 28 | 9 | 122 | 80.6 | 0.033 | 0.302 |
| S | 32 | 10 | 133 | 81.6 | 0.033 | 0.305 |
| Fe | 56 | 11 | 111 | 98.9 | 0.030 | 0.353 |

* For 440 km/s solar-wind speed and 23kV post-acceleration
** Measured by solid-state detector

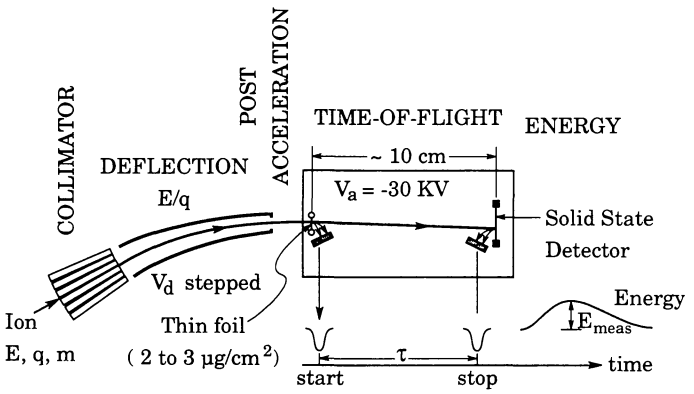


FIGURE 1. Schematic of the measurement technique used in the SWICS, showing the functions of each of the five basic elements.

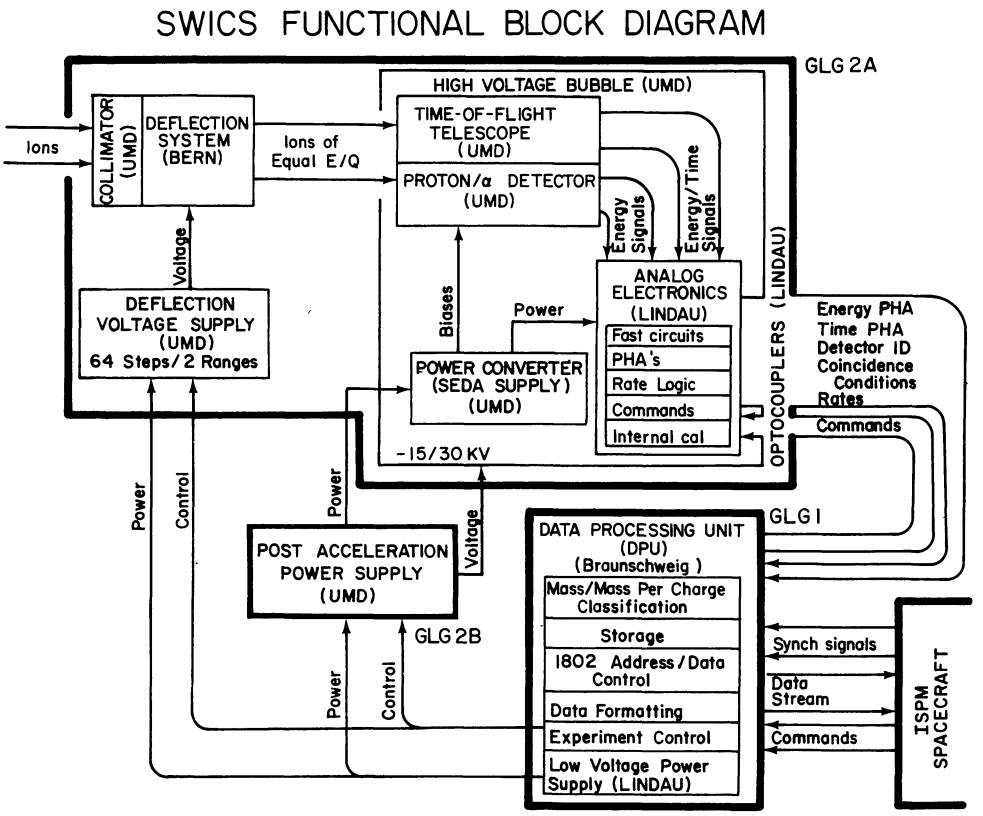


FIGURE 2. Functional block diagram for the SWICS experiment. The three separately packaged units GLG-1 (DPU), GLG-2A (sensor) and GLG-2B (post-acceleration supply) are shown as solid-border boxes. Subsystems, and the responsible institutes, are indicated within each of the three units. The flow of ions as well as signals, power and control among the subsystems and units is also shown.

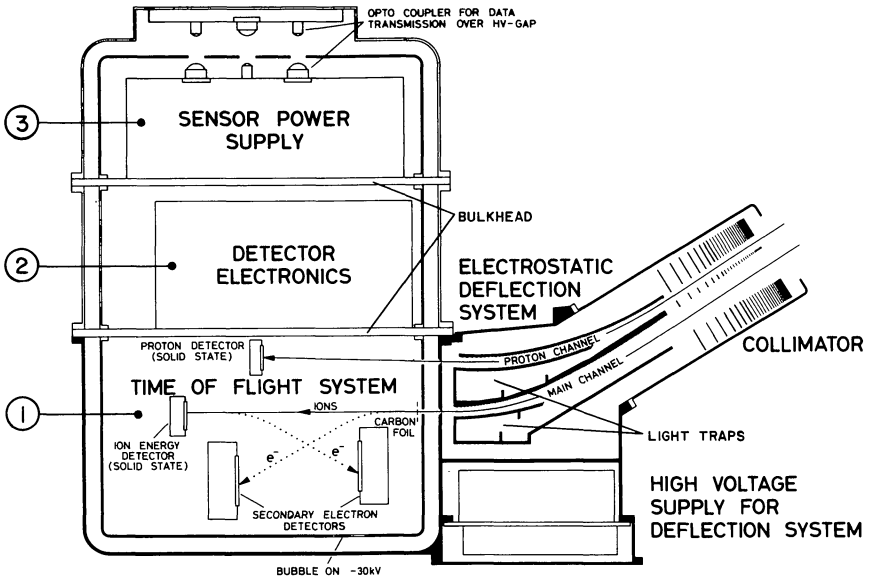


FIGURE 3. Cross-section of the SWICS sensor (GLG-2A) showing the collimator, the two-channel deflection system and its deflection power supply, the time-of-flight system and proton/helium detector, analog electronics, sensor bias and power supply, and opto-couplers for digital data transmission. The three inner compartments are supported by two bulkheads and are maintained at the post-acceleration voltage (− 15 kV to − 30 kV). The outer diameter of the cylindrically shaped outer housing is 15 cm.

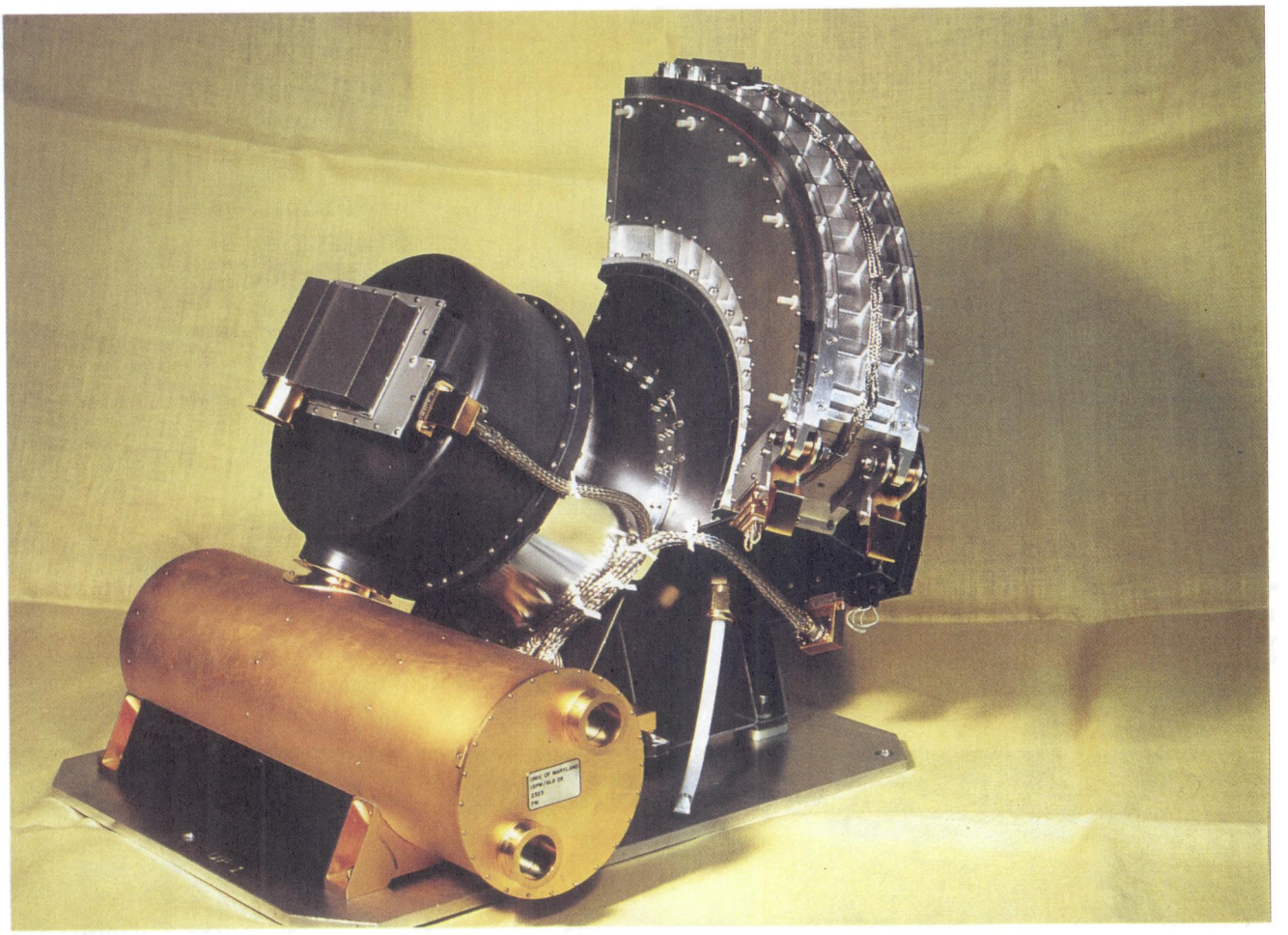

FIGURE 4. The SWICS experiment.

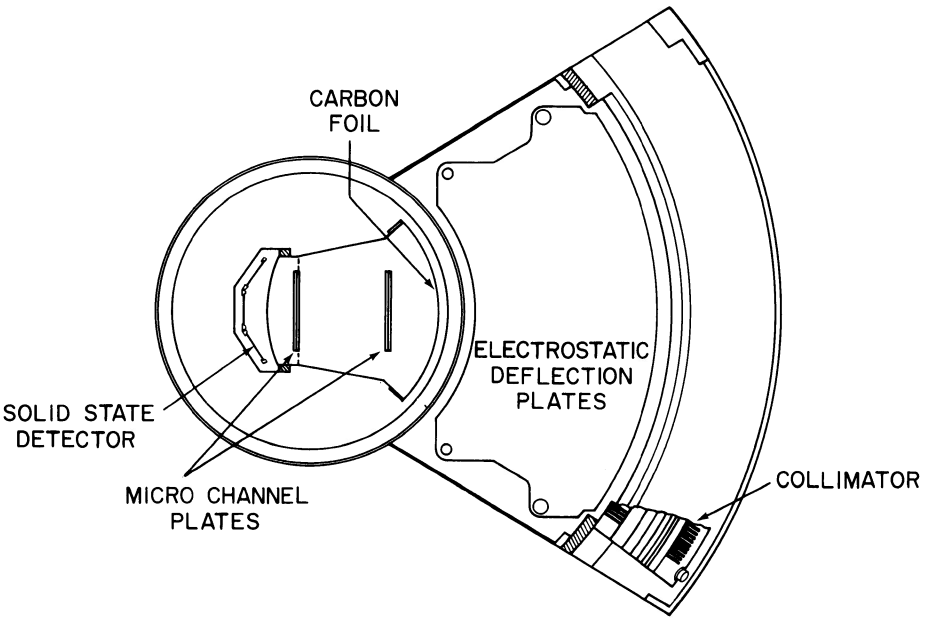


FIGURE 5. Top view of the SWICS sensor, showing the cross-section of the time-of-flight telescope, and the positions of the three solid-state detectors, two microchannel plate assemblies, and the curved, grid supported carbon foil. The shapes of the deflection plates and the individual plates of the collimator are also shown.

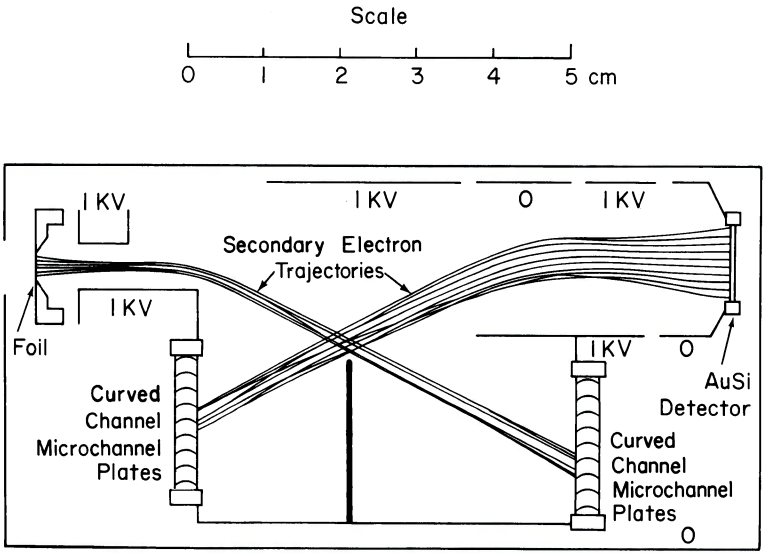


FIGURE 6. Cross-section of the SWICS time-of-flight vs energy telescope showing computer-generated trajectories of secondary electrons emitted from the carbon foil and solid-state detector. The front surface of each of the two curved-channel microchannel plates (MCP) is biased sightly negatively with respect to the housing to repel low-energy (<100 eV) secondary electrons. A physical partition between the two MCPs prevents secondary electrons from one MCP triggering the other.

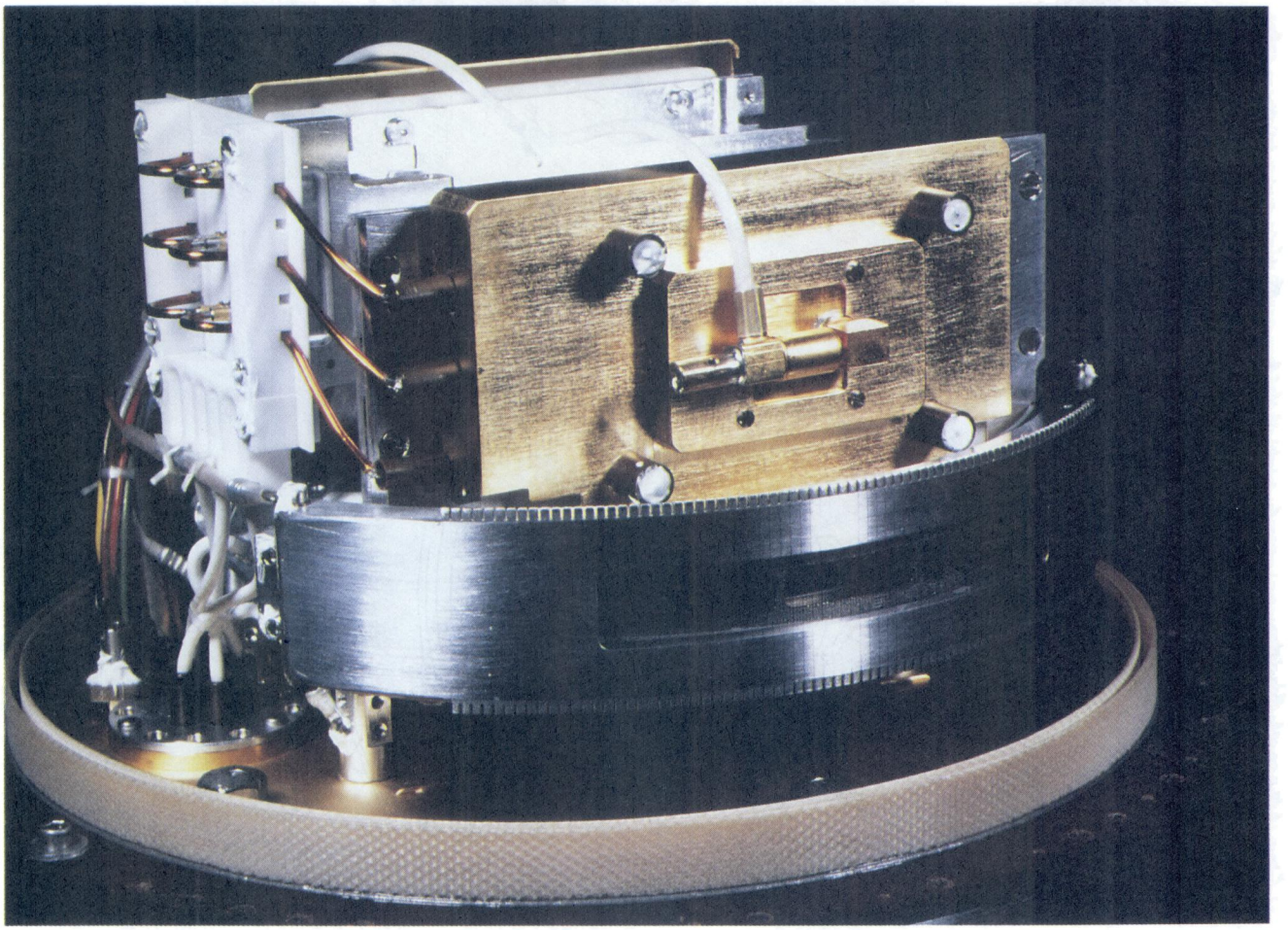

FIGURE 7. The SWICS time-of-flight vs energy telescope.

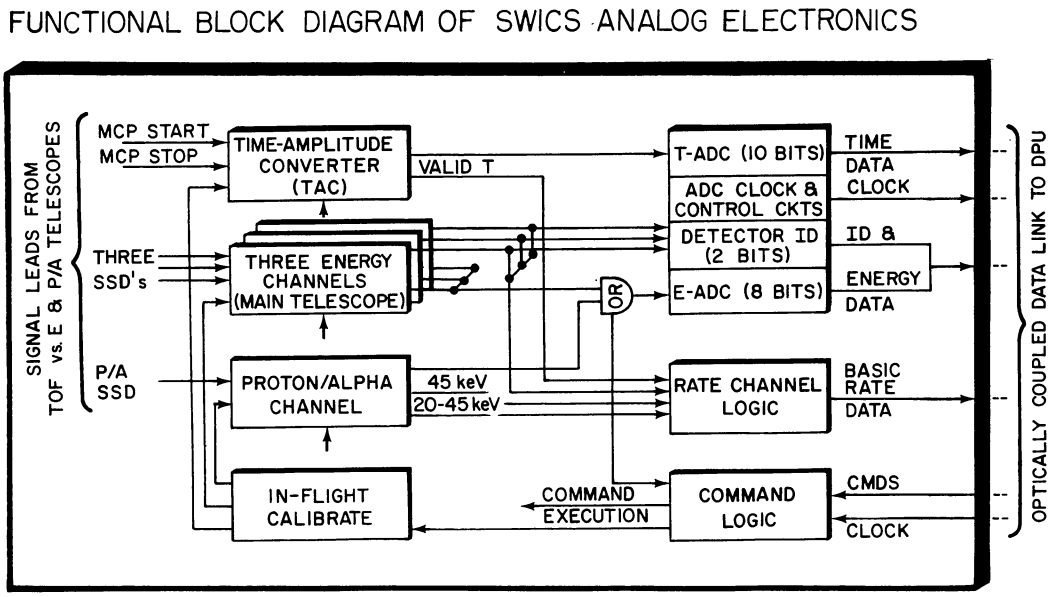


FIGURE 8. Functional block diagram of the SWICS analog electronics consisting of four energy channels (preamplifier, shaping amplifiers, discriminator) fed by the three TOF telescope solid-state detectors (SSD) and the proton/helium SSD, a time-to-amplitude converter (TAC), inflight calibration circuits providing energy and timing pulses, rate logic and buffering, command logic, and time ($T$) and energy ($E$) Analog-to-Digital Conversion (ADC) circuits. 24-bit pulse-height/detector ID words and six rates are transmitted via opto-coupler links to the Data Processing Unit (DPU).

$$M(E,T) = M_0(E_0,T_0) + \partial M/\partial E\,(E_0,T_0)\times\Delta E + \partial M/\partial T(E_0,T_0)\times\Delta T$$

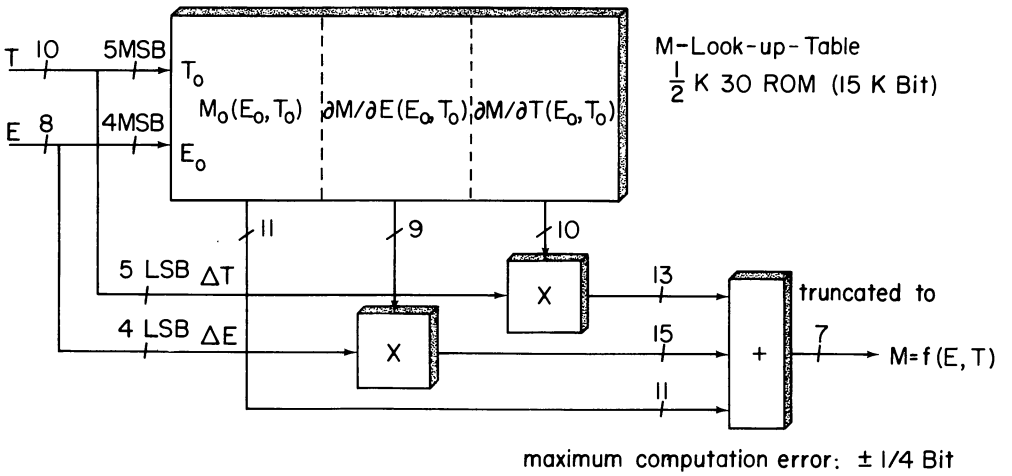


FIGURE 9. Block diagram illustrating the operating principle of the SWICS mass classification scheme. A 15 kbit ROM look-up table stores coefficients for the Taylor expansion which are derived from SWICS sensor calibration data. The most significant bits of the time and energy pulse heights are used to select the three appropriate coefficients from the table. Table-look-up multiplication and addition using the three coefficients and the least-significant bits of the pulse heights complete the computation of the ion mass.

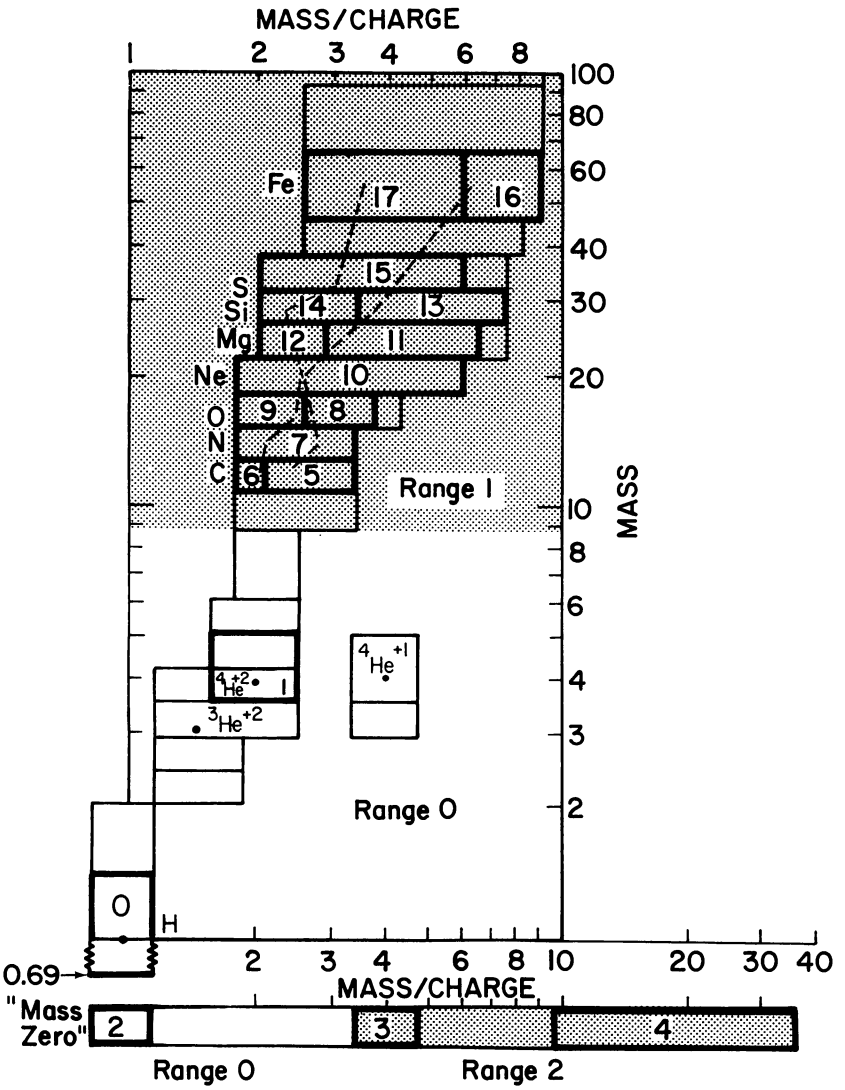


FIGURE 10. Location of the 18 matrix-rate box boundaries (heavy borders) in the $m$ vs $m/q$ plane. The "mass-zero" line corresponds to ions (e.g. $O^+$) that had insufficient energy to trigger the solid-state (energy) detector. The three priority range correspond to $m < 8.7$ or "mass-zero" with $m/q < 3.3$ (Range-0), the shaded region with $m > 8.7$ (Range-1), and the shaded region on the "mass-zero" line with $m/q > 3.3$. Dashed curves represent the expected locus of dominant charge states for coronal temperatures of $2 \times 10^6$ K (left curve) and $10^6$ K (right curve). Each of the boxed regions (both heavy and light borders) is further divided into logarithmic evenly-spaced $m/q$ bins of 3% in the Range 1 portion and 6% in the rest. These bins form a large portion of the 512 matrix elements.

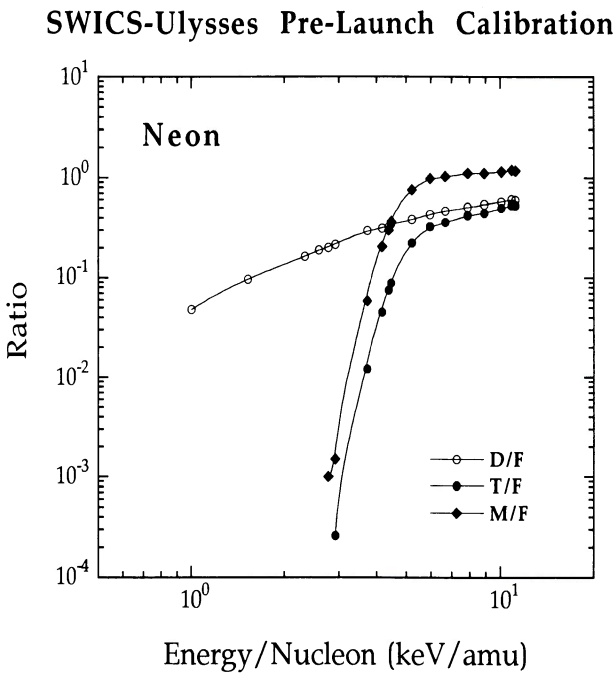


FIGURE 11. Calibration data for the flight microchannel plates that were taken at the University of Bern acceleration facility in May 1990. Shown here are the relative efficiencies for an incident Neon beams for the Double Coincidence Rate (D), the Triple Coincidence Rate (T), and the Main Solid State Detector Rate (M) relative to the start signal (Front Seda Rate, F). The ratios are plotted against total ion kinetic energy/nucleon, after post acceleration. The rapid drop off at low energies for the $M/F$ and $T/F$ ratios results from the 40 keV threshold of the solid state detector.

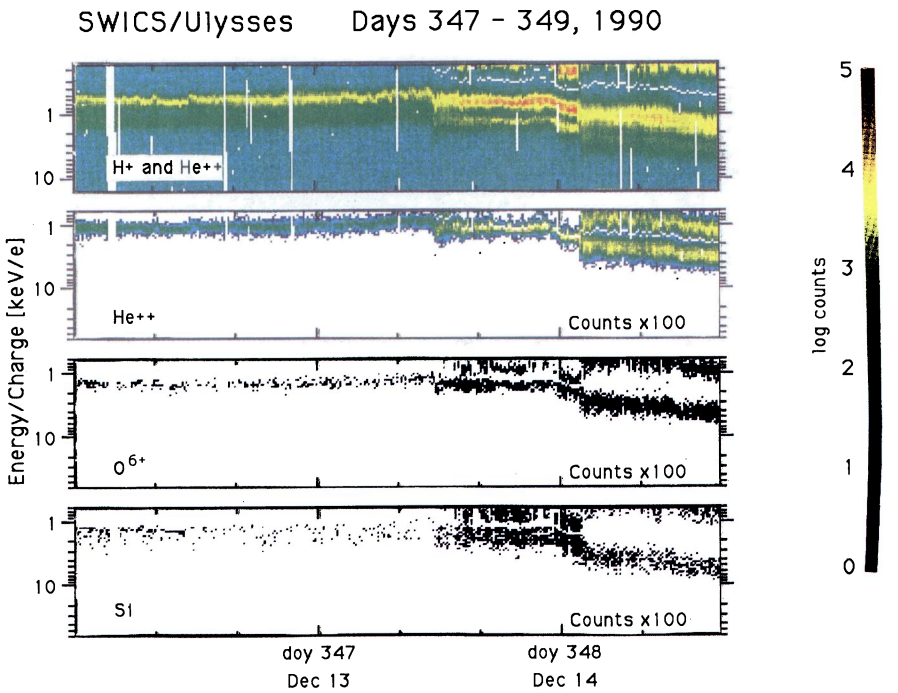


FIGURE 12. Energy vs time color spectrogram of counts per voltage step from the solid state detector of the H/He channel (top panel), and from matrix rates recording primarily $He^{++}$, $O^{6+}$, and Si for days 347-349 (Dec 13-15) 1990. In these overview plots, changes in density (color), bulk speed and kinetic temperature of representative solar wind ions are easy to see. The double traces, seen best in the lower two panels, are the result of the step reversal mode. (See text for explanation).

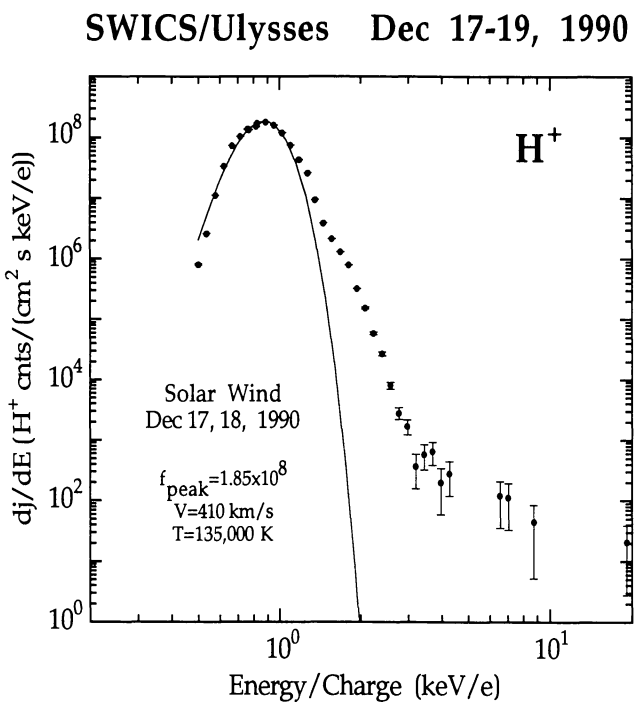


FIGURE 13a.

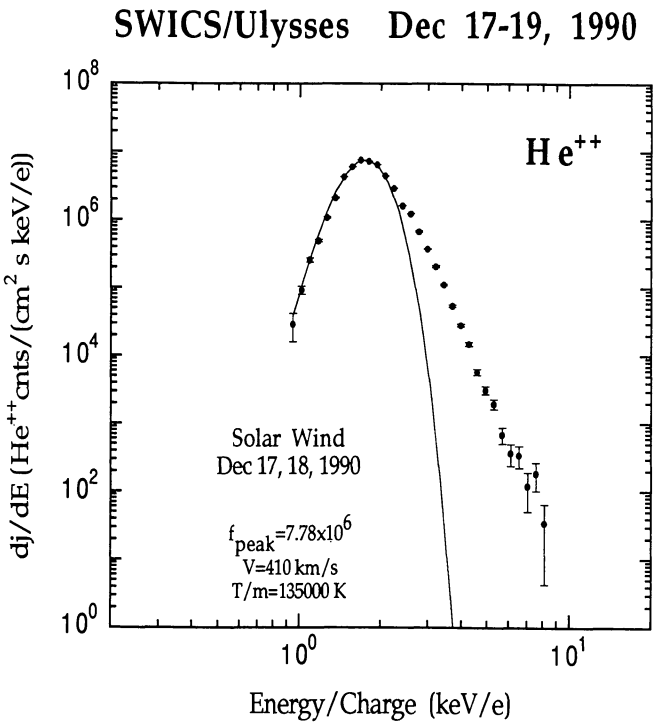


FIGURE 13b.

FIGURE 13. Differential energy per charge spectra of $H^+$ and $He^{++}$ illustrating the $\sim 10^8 - 10^9$ dynamic range of the SWICS. A single convected maxwellian, $dj/dE = j_0 \exp\left[-(v-V)^2/(2kT/m)\right]$, fits the peaks of both spectra, indicating that at this time solar wind protons and alpha particles had the same bulk speed of 410 km/s and temperature/mass of $13.5 \times 10^4$ K. A well-developed high energy, non-maxwellian tail is observed in the spectra of $H^+$, and $He^{++}$.

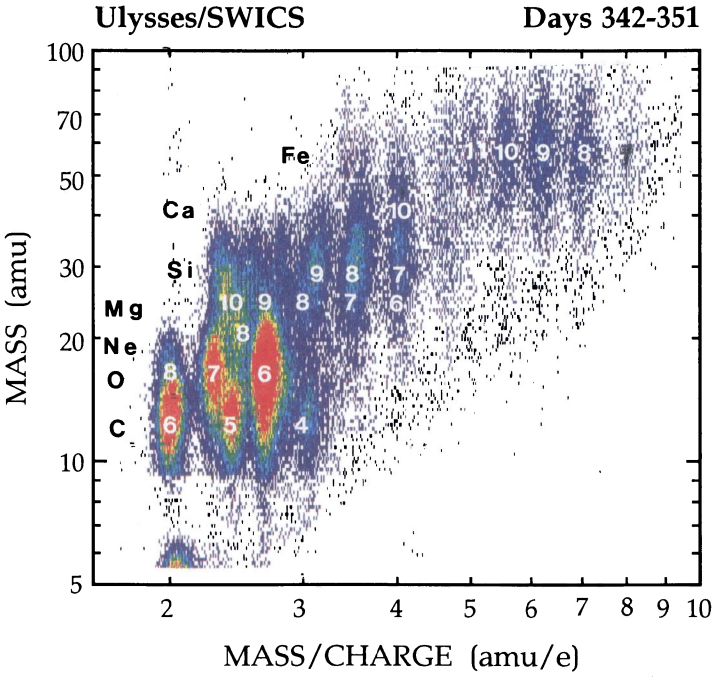


FIGURE 14. Display of the mass vs mass per charge distributions of solar wind ions derived from the raw energy and time-of-flight pulseheight data collected by the SWICS during the 8 to 17 Dec, 1990 time period. The mass and mass/charge values were computed on ground using algorithms identical to those employed by the instrument to do on-board classification of solar wind ions. The color coded density profiles (red: greater or equal to 30 counts/bin) show well-resolved peaks of the major solar wind heavy elements and their dominant charge states (e.g. $C^{6+}$, $C^{5+}$, $O^{7+}$, $O^{6+}$, $Si^{9+}$, $Si^{8+}$, $Si^{7+}$, $Fe^{11+}$, $Fe^{10+}$, $Fe^{9+}$, $Fe^{8+}$). The relative abundances of the various charge states of elements that can be derived from data such as shown here may be used to derive the temperatures and temperature profiles of the solar corona.

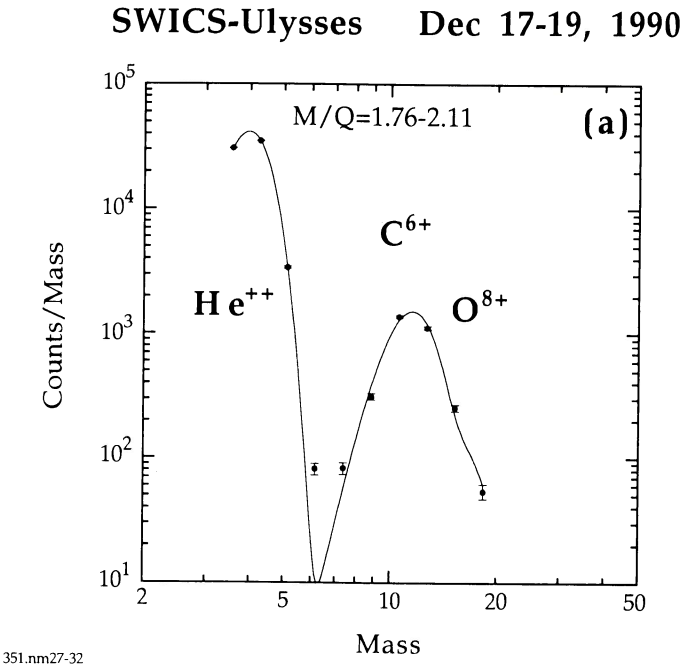


FIGURE 15a.

FIGURE 15. Examples of mass and mass per charge distributions extracted from matrix element data [panel (a)] or from mass vs mass/charge matrices (such as shown in Figure 14) [panels (b)-(d)] with the SWICS at a post-acceleration voltage of 22.9 kV. These distributions illustrate the mass and charge resolution capabilities of the SWICS. We note that the mass and mass/charge resolution is the same, regardless of solar wind flow conditions. The mass resolution, however, will improve with higher post-acceleration voltage.

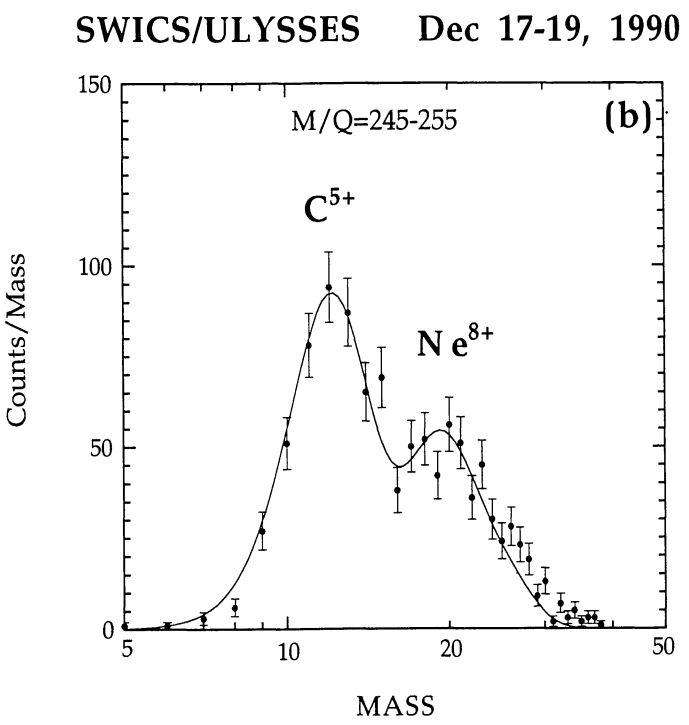


FIGURE 15b.

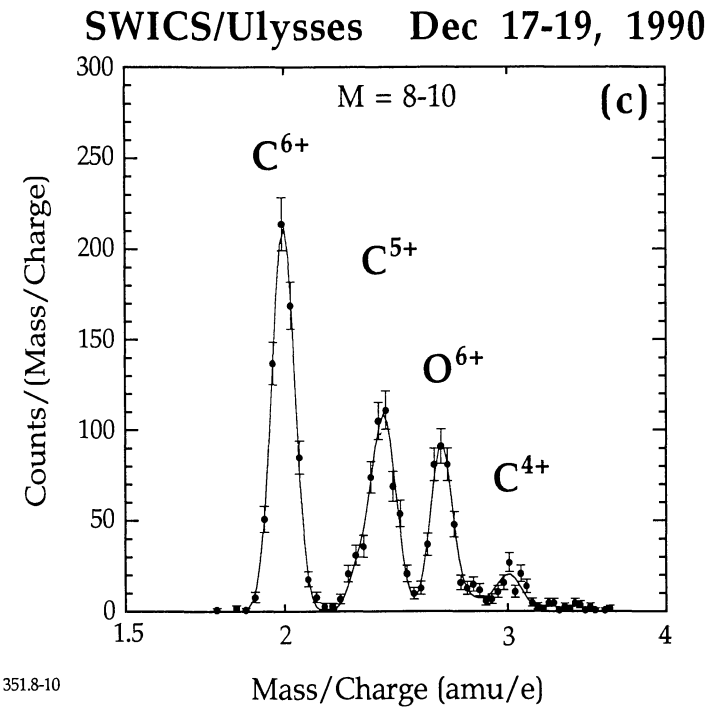


FIGURE 15c.

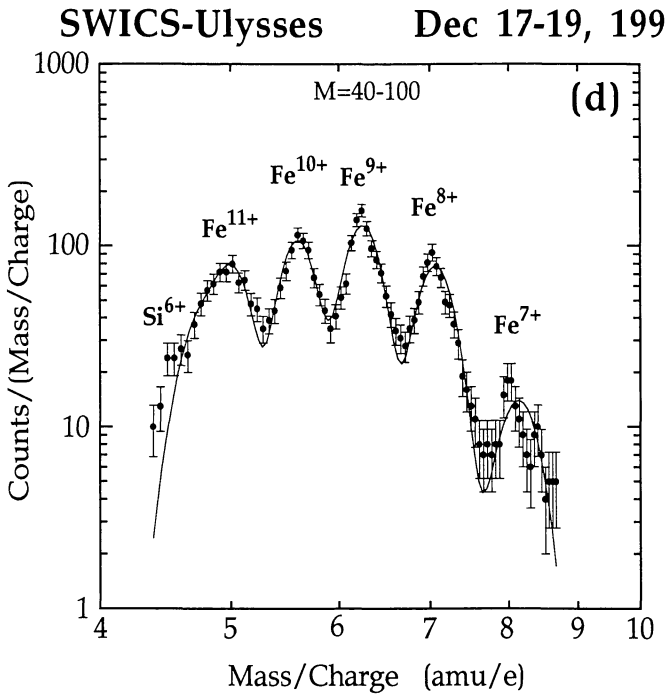


FIGURE 15d.

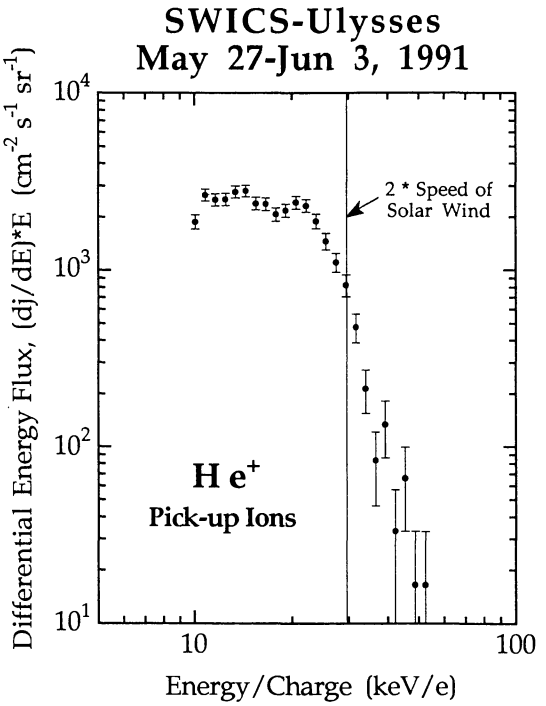


FIGURE 16. Differential energy flux spectrum of $He^+$ ions observed on May 27 June 3, 1991. The absolute flux values of this preliminary spectrum may have systematic uncertainties of about a factor of two. This spectrum is similar to that observed for $He^+$ pick-up ions by Moebius *et al.* (1985), with a sharp cut-off at twice the measured solar wind speed of about 650 km/s.